Experimental Study of Porous Treatments for Aerodynamic and Aeroacoustic Purposes

Syamir Alihan Showkat Ali*, Mahdi Azarpeyvand†
Faculty of Engineering, University of Bristol, BS8 1TR, UK
Carlos R. Ilário da Silva‡
Embraer, São José dos Campos, 12227-901, Brazil

This paper is concerned with the noise generation mechanism from blunt trailing-edges and the use of porous treatments for reducing the radiated noise, and stabilizing the vortex shedding and the wake region. Experiments have been carried out for a flat plate with and without porous trailing-edges. To gain a better understanding of the underlying physics of the noise generation mechanism and the effects of porous trailing-edges, velocity measurements have been carried out within the boundary layer and wake. Surface pressure fluctuation measurements have also been performed near the plate trailing-edge. Results have shown that the use of porous surfaces leads to an increase of the shear stresses in the near wall region of the boundary layer but significant reduction of the energy content of the larger turbulent structure in the outer layer. The PIV results have also shown that the porous trailing-edge can delay the vortex shedding and significantly increase the vortex formation length, resulting in a very low turbulent near wake region. The surface pressure measurement results indicate that the use of porous treatment increases the broadband energy content of the surface pressure fluctuations globally in the whole frequency ranges, but, also effectively eliminates the vortex shedding frequencies. A noticeable reduction can also be observed in the lateral coherence of the turbulent structure in the case of porous trailing edges. The results demonstrate that porous treatments can be used for stabilizing boundary layer, wake flow and noise reduction purposes.

Nomenclature

L_x	fore-body length $[mm]$
L_z	spanwise length $[mm]$
h	plate thickness $[mm]$
κ	permeability $[m^2]$
U_∞	free stream velocity $[m/s]$
U	mean velocity $[m/s]$
U_{rms}	root mean square velocity $[m/s]$
C_d	drag force coefficient
δ	99% boundary layer thickness $[mm]$
Re	Reynolds number
PPI	pores per inch
St	Strouhal number
ϕ_{uu}	power spectral density of velocity fluctuations $[dB/Hz]$
ϕ_{pp}	power spectral density of pressure fluctuations $[Pa^2/Hz]$
γ^2	Magnitude squared coherence

*Ph.D Student, Department of Mechanical Engineering, ss14494@bristol.ac.uk
†Senior Lecturer and Royal Academy of Engineering Research Fellow, Mechanical Engineering, m.azarpeyvand@bristol.ac.uk
‡Technology Development Engineer, Embraer, Sáo José dos Campos, Brazil carlos.ilario@embraer.com.br

x, y, z cartesian coordinates

I. Introduction

The use of porous materials for flow control in aerodynamics and aeroacoustics has received much attention in experimental and numerical research studies in the past. The use of porous materials for passive-typed control system of flow-induced noise and vibrations has been shown to be quite effective for airfoils, bluff and blunt bodies in many engineering applications. Passive control methods include O-rings,[1] dimple,[2] longitudinal groove,[3] splitter plate,[4] serrations,[5–11] morphing,[12,13] porous materials,[14–17] surface treatments.[18,19] Porous treatments have been of much interest amongst the other passive treatments. To date, prior research in this area has shown that careful implementation of porous materials can lead to robust flow control, turbulence stabilization and significant noise reduction.

Among the many applications of aerodynamic and aeroacoustic study, blunt trailing-edge noise has been an important topic due to the wide range of engineering applications they feature in. The blunt trailing-edge bodies have been widely used for numerous aerodynamic applications, such as the flatback airfoils and the wind turbine blades. The blunt body is known to have superior lift characteristics and structural improvement, however the use of blunt trailing-edges also results in structural vibration and increase of drag, which is due to the undesirable vortex shedding generated by the blunt trailing-edge.[20] This typed of the body also causes sound generation, specifically the airfoil self-noise. Turbulent boundary layer noise generation at the trailing-edge has gotten extensive consideration in the course of recent years. The development of a noise prediction method has been successfully detailed by Brooks and Hodgson[21] for the case of turbulent boundary layer flow. Their studies showed that the resulting noise can be overall estimated using the relation of the turbulent flow field to the surface pressure energy spectra, convective wall speeds and the cross spectra using NACA 0012 airfoil. This approach has been also applied by Brooks *et al.*[22] and Roger and Moreau[23] to understand the relationship of the airfoil surface pressure and the trailing-edge noise. In regards to blunt bodies, the trailing-edge noise is predominantly consists of the broadband and tonal noise, which are caused by the eddies shedding from the blunt trailing-edges and the scattering of the convective eddies at the trailing-edge vicinity. Hoerner and Borst[24] showed that blunt trailing-edge on symmetric G-490 airfoil have a significant increase in the maximum lift coefficient and maximum-thickness to chord ratio (t/c) using a constant chord Reynolds number of 500,000. Bearman and Tombazis[25,26] in their study involving spanwise periodical protrusions at the blunt trailing-edge profiles resulted into 34 % reduction of drag. This is related with the mitigation of vortex shedding which was identified with the advancement of three dimensional structures in the shear layer. Moreover, the impact of blunt trailing-edge airfoil sections for lower Reynolds number have been considered by Sato and Sunada.[27] They have tested five airfoil sections at three different Reynolds number (33,000, 66,000 and 99,000) for the aerodynamic forces and flow visualization studies. The results indicate that at low Reynolds number, the total drag is reduced and the maximum lift had been increased. In addition, the maximum lift to drag ratio has increased and the linearity of the lift curve has improved. A combination of surface pressure taps, hot-film anemometry and laser droplet velocimetry have been used by Thompson and Lotz[28] to further study the flow around a blunt trailing-edge airfoil. It was observed that the vortex shedding occurs in the wake at Strouhal number of 0.21 for all Reynolds number tested, which influences the overall base pressure, skin friction and the drag performance of the airfoil. Besides that, Deshpande and Sharma[29] have investigated the vortex flows behind a segmented blunt trailing-edge with different spanwise, resulting into suppression of the periodic von Kármán vortex shedding in the near wake behind the blunt body. A comprehensive experimental study on the vortex shedding control from a blunt trailing-edge using plasma actuator in laminar boundary layer regime had been conducted by Nati *et al.*[30] using hot-wire anemometry and high speed PIV. The results indicate the suppression of von Kármán vortex in the developing wake region where the analysis shows a reduction in the vortex shedding frequency peak during steady plasma actuation by 10 dB.

Interest in blunt airfoil, also called "thick airfoil" in several studies[31,32] have shown significant improvement in the lift performance for a wide range of Reynolds number applications. Standish and Van Dam[31] also concludes that the blunt airfoils enable notable portion of pressure recovery to take place in the wake which consequently generate steep adverse pressure gradients leading to the premature flow separation of the airfoil. Bruneau *et al.*[33] had numerically studied the use of porous interfaces on the blunt bodies in order to regularise the flow and reduce drag. Results had shown the capability of the porous layer in re-

ducing the pressure gradient near wake up to 67 % and considerable drag reduction up to 45 %. The effect of porous treatment on the blunt trailing-edge of a flat plate have been investigated by Bae *et al.*[34] The three-dimensional turbulent flow over the blunt trailing-edge flat plate has been studied using incompressible large eddy simulation (LES) and linearized perturbed compressible equations (LPCE) with Reynolds number of 130,000 and M=0.06. It was found that the porous surface weakens the pressure fluctuations near the trailing-edge for separate flow cases, which results in a noticeable noise reduction of up to 10 dB over a wide range of frequency. The broadened tonal noise also have been reduced significantly up to 13 dB by breaking the wall pressure fluctuations space correlation length. Bae and Moon[35] have studied the effects of permeable material surfaces on turbulent noise generated by a blunt trailing-edge of flat plate using LES on the domain rigid on LPCE, and the results have shown significant reduction of the broadband noise over a wide range of frequencies. Schulze and Sesterhenn[36] have studied the use of porous material for trailing-edge noise control and developed a methodology to maximise the noise reduction by optimizing the porous material. Koh *et al.*[37] investigated the trailing-edge noise reduction of a flat plate using LES and Acoustic Perturbation Equations (APE). The results showed that the porous surface changes the turbulence structures in the shear layer, reduces the sound pressure level up to 3-8 dB and influences the tone generation by significant reduction in the peak by 10 dB. In addition, Zhou *et al.*[38] developed a discrete adjoint-based optimization framework to obtain the optimal distribution of porous material on trailing-edge of a flat plate using an LES solver. The results obtained indicated that there is a possibility of minimizing the turbulence near the trailing-edge and therefore controlling the noise generation at the trailing-edge.

As reviewed above, the viability of using porous materials as a passive method to control the flow and weaken aero-acoustic type noise sources of the blunt bodies has been verified numerically in several research works over the past decade, however no experimental work has been conducted. In some more recent research activities, it has been tried to further improve the effectiveness of such porous treatments by optimizing the shape and mechanical properties of the porous section, *i.e.*, porosity and permeability. In this paper, a passive flow control method based on porous material for blunt trailing-edge has been investigated experimentally to further understand the effectiveness and the underlying physics of porous treatments. Our particular focus is on assessing and understanding the complex phenomena of the turbulent flow attributed by the blunt TE plate by revealing the characteristics of the turbulent structure, and particularly the vortex formation, boundary layer profile and the surface pressure measurement. The experimental setup and wind-tunnel tests are described in Sec. II. The results and discussions are detailed in Sec. III.

II. Measurement Setup

Flow experiments have been performed for a blunt flat plate, with solid and porous trailing-edges in the open-jet wind tunnel of the University of Bristol (UoB), see Fig. 1. The wind tunnel has a test-section with a diameter of 1.1 m and test-section length of 2 m. Results have been obtained for flow velocities of up to 26 m/s, corresponding to the Reynolds number of $Re_{L_x} = 5.8 \cdot 10^5$, with incoming flow turbulence intensity of below 0.05 %. To properly understand the effect of the TE properties (solid and porous), various aerodynamic measurements have been performed, such as the aerodynamic loads, boundary layer growth, wake development and surface pressure fluctuations.

A. Blunt trailing-edge model design and configuration

The model of the blunt trailing-edge flat plate rig is shown in Fig. 1. The plate has a fore-body length of $L_x = 350\ mm$, spanwise length of $L_z = 715\ mm$ and thickness of h =20 mm. The corresponding aspect ratio of the flat plate is $AR_x = L_x/h = 17.5$. The model in the open-jet wind tunnel gives a blockage ratio of 1.8 %, which is expected to have negligible effect on the results obtained.[39] The flat plate has an elliptical leading edge in order to prevent strong adverse pressure gradient and large flow separation at the beginning of the plate. To ensure the presence of vortex shedding, the ratio of the trailing-edge height and the boundary layer displacement thickness obey, $h/\delta^* > 0.3$, where h is the plate thickness and δ^* is the boundary layer displacement thickness at the trailing-edge.[40] The bluntness ratio was found to be significantly larger than 0.3 in our experiments, ensuring the existence of vortex shedding. In order to reach a well-developed turbulent flow before the porous section, a 25 mm wide sand trip was applied just aft of the leading edge with a thickness of approximately 0.6 mm and grit roughness of 80. The trip was placed on both sides of the plate. The porous section is placed at the trailing-edge with a width (L_{px}) and length

of 50 mm and 500 mm, respectively, see Fig. 1. To ensure two dimensional flow over the span, rectangular side-plates of dimension 425 mm by 80 mm, with sharpened leading edges with an angle of 20° were mounted on the test apparatus. The side-plates extend approximately $1.25h$ upstream of the leading edge and $2.5h$ downstream of the trailing-edge.

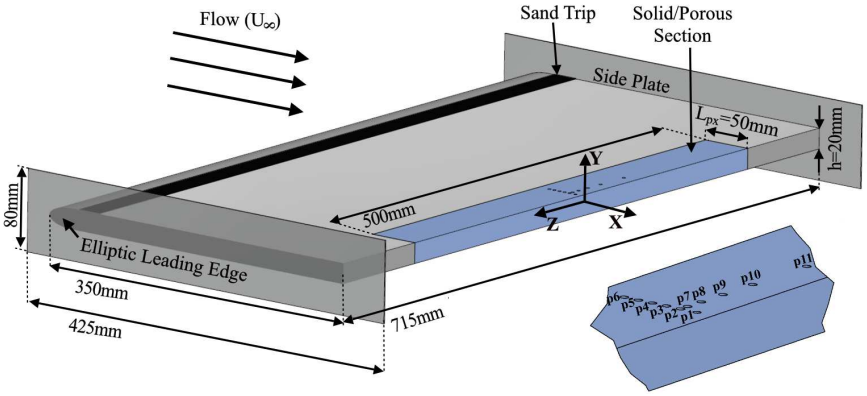

Figure 1: Flat plate blunt trailing-edge schematic with major dimensions and the coordinate axis

B. Porous Samples Analysis

Two metal foams with the PPI (pores per inch) of 25 and 80 have been chosen for this study. It is known of prior experimental[41,42]and computational[43,44] works that the effectiveness of porous materials as a flow control technique depends heavily on their porosity and permeability. The porosity of the porous samples were captured by using a Nikon XT H 320 LC computed tomography scanner and the data obtained were then visualized and analyzed using the Volume Graphics (VGStudio MAX 2.2) software. The porosity then is calculated as $\varphi = V_V/V_T$, where φ is the porosity, V_V is the volume of void space and V_T is the total volume of the sample. The $3D$ image of the porous structure is shown in Fig 2. The porosity values for porous 25 PPI and 80 PPI are 90.92 % and 74.76 %, respectively.

The permeability (κ) of each porous material used in this study was measured using a permeability test apparatus over a wide range of Darcy velocities. The permeability rig is comprised of a long $2.5m$ tube, with square cross-section, equipped with static and dynamic pressure taps, with the porous sample being placed $1.2m$ from the inlet. Experiments were performed on porous sample inserts of 80×80 mm and thickness of 10 mm. Static pressure taps were flush mounted on the inner surface of the apparatus, perpendicular to the airflow, either side of the porous sample and the pressure measurements were obtained using the MicroDaq Smart Pressure Scanner-32C. The permeability factor (κ) can then be found using Dupuit-Forchheimer equation,[45] $\triangle p/t = \mu/\kappa\nu_D + \rho C\nu_D^2$, where $\triangle p$ is the pressure drop across the sample, t is the thickness of the sample, ρ is the density of fluid, C is the inertial loss term, ν_D is the Darcian velocity, defined as the volume flow rate divided by cross sectional area of sample. The permeability values for porous 25 PPI and 80 PPI were found to be 8.19×10^{-8} m^2 and 76.88×10^{-8} m^2, respectively, implying that the porous 25 PPI has larger porosity and permeability coefficient than porous 80 PPI.

C. Force Balance Measurement Setup

All steady aerodynamic measurements were performed in the open-jet wind tunnel facility of the University of Bristol. The drag force measurements were collected using an AMTI OR6-7-2000 force-plate unit. The flat-plate rig was mounted on a set of steel extension arms with symmetrical tear-drop shape to minimise any additional drag forces acting on the rig. The force-plate was load tested prior to the experiment. The generated voltage signal from the force-plate passed through an AMTI MSA-6 strain gauge amplifier and the final data from this unit was captured using a LabView system. A detailed uncertainty and data independency test has been conducted using different sampling frequencies and the best sampling frequency of 45 Hz with the least uncertainty value[46] has been chosen for the measurement. Measurements were carried out for 30 seconds at each velocity, data have been collected for velocities between 6 m/s to $26m/s$ wind

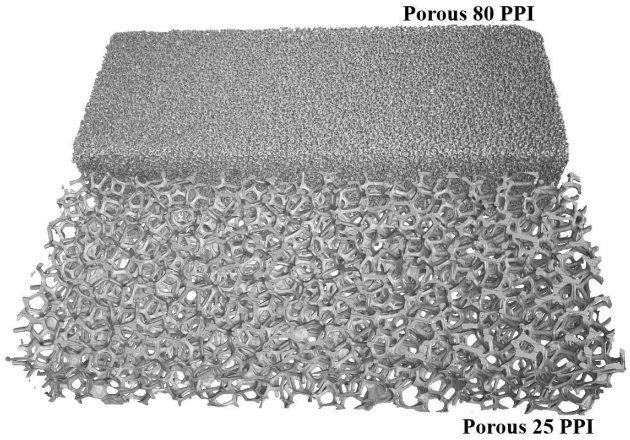

Figure 2: Metal porous geometry obtained using the x-ray computed tomographic (CT) scanning

speed with $2m/s$ increments. The speeds were set such that all data were recorded once the deviation of the velocity was 0.2 m/s or less. To ascertain the repeatability of the measurements, repeated tests were conducted and the uncertainty was found to be less than 1 %.

D. Hot-wire Anemometry Setup

The boundary layer and wake flow measurements were carried out using single-wire Dantec 55P16 probes, with a platinum-plated tungsten wire of 5 μm diameter and 1.25 mm length, and cross hot-wire Dantec 55P51 probes with 5 μm diameter and 3 mm length platinum-plated tungsten wires. The probes were operated by a Dantec StramlinePro frame with CTA91C10 modules. The signals were low-pass filtered by the StreamlinePro frame with a corner frequency of 30 kHz before they were A/D converted, with an applied overheat ratio of 0.8.[47] The data has been acquired by a National Instrument 9215 type 4-channel module, with a sampling frequency of 40 kHz. The hotwire measurements have been taken for 15 seconds at each location. The calibration of the probes were performed using the Dantec 54H10 type calibrator. The X-wire probes were also calibrated using the directional calibration to obtain the pitch and yaw coefficients on the same calibrator unit. The calibration process was performed before and after each measurement and the polynomial constants were averaged prior to post processing of the results. The error analysis of the velocity values obtained by the use of the hot-wire probes was performed based on the manufacturer description.[47] The uncertainty derived from the measured velocity signals were found to be within 1 %. The hot-wire probes were installed on a two-axis ($x-y$) ThorLabs LTS300M traverse system, covering a 300mm by 300mm domain with typical minimum positioning accuracy of 5 μm.

E. Particle Image Velocimetry Setup

The particle image velocimetry (PIV) technique was used to obtain time-averaged velocity over the xy plane. All measurements were performed in the low turbulence closed-circuit wind tunnel at the University of Bristol of closed return type with an octagonal test section (0.8 m × 0.6 m × 1 m) with a maximum flow speed of 100 ms^{-1}. The wind tunnel has a turbulent intensity of 0.05 % at 20 ms^{-1}. The blunt flat plate in the tunnel gives a blockage ratio of 3 %, which will not have significant effect on the aerodynamic behaviour of the model.[48] A dual-cavity laser of 200 mJ Nd:YAG with a wavelength of 532 nm was used to produce 1 mm laser sheet thickness with the time interval between each snapshots of 25 μs with a repetition rate of 5 Hz to attain maximum amount of particles in the interrogation window. A mixed Polyethylene glycol 80 based seeding was used in the flow, producing particle size from 1 and 5 μm. A total of 1600 image pairs were captured using a FlowSense 4 MP CCD camera with a resolution of 2072 x 2072 pixels for each case and used to compute the statistical turbulence quantities. The measurements were made for a field view of 158 mm × 158 mm, which corresponds to a domain of 7.9 h × 7.9 h in the streamwise and spanwise directions. The iterative process yield grid correlation window of 32 × 32 pixels with an overlap of 50 %, resulting in a facial vector spacing of 0.43 mm.

F. Surface Pressure Measurement Setup

To better understand the boundary layer characteristics, surface pressure fluctuations measurements have been performed using an array of miniature Knowles FG-23329-P07 type-transducers. These miniature transducers are 2.5 mm in diameter and have a circular sensing area of 0.8 mm and have regularly been used in aeroacoustic applications, particularly for boundary layer surface pressure measurements,[49,50] due to their small size and good frequency response. Corcos[51] stated that the pressure fluctuations at frequencies where the wavelength magnitude is smaller than the transducer diameter are spatially integrated, and thereby attenuated. In order to eliminate the errors present in the wall pressure spectrum measurement, a small sized pinhole transducers sensing area are employed. The trailing-edge section of the rig was instrumented with 11 flush mounted miniature Knowles-transducers (FG-23329-P07) under a pinhole mask of 0.4 mm diameter. According to the studies carried out by Gravante *et al.*,[52] to avoid attenuation due to the pinhole size, the pinhole diameter should be in the range of $12 < d^+ < 18$ for frequencies up to $f^+ = f\nu/u_\tau^2 = 1$. The pinhole diameter (d) to the wall unit ν/u_τ ratio, *i.e.* d^+=$d\ u_\tau/\nu$, determines the significance of the pressure fluctuations attenuation. The mask pinhole used for the current study for the free-stream velocity of 20 m/s, gives a non-dimensionalized diameter range of $12 < d^+ < 19$, which is not far from the pinhole diameter suggested by Gravante *et al.*[52] The uncertainty obtained from the surface pressure measurements were found to be within $\pm$0.5 dB with 99 % of confidence level. The data has been acquired by a National Instrument PXIe-4499 type, with a sampling frequency of 2^{16} Hz and measurement time of 32 seconds. The transducers are arranged in the form of an L-shaped array in the streamwise and spanwise directions (see Fig. 1). The transducers located in the spanwise direction will be used for the calculation of the spanwise length-scale of boundary layer structures, while the transducers employed in the streamwise direction provide information on the evolution of the turbulence structures as they move downstream towards the trailing-edge and their convection velocity. The pressure transducers, $p2$ to $p6$, are equally spaced in the streamwise direction, while the transducers, $p7$ to $p11$, are unequally spaced in the spanwise direction and placed 14 mm upstream of the trailing-edge to maximize the number of correlation distances ($\triangle$z) between the transducers in furtherance of capturing the spanwise coherence at high and low frequencies. The detailed locations of the miniature transducers on the detachable trailing-edge part are shown in Fig. 1 and summarized in Table 1.

Table 1: Positions of the pinhole transducers on the trailing-edge

Position	Transducers Number	Axial locations, x (mm)	Transverse locations, z (mm)
Streamwise	p1, p2, p3, p4, p5, p6	-7, -14, -20, -26, -32, -38	0.0
Spanwise	p7, p8, p9, p10, p11	-14	4.6, 13.4, 27.4, 46.6, 81.4

III. Results and Discussion

A. Steady Drag Coefficient

A basic but fundamental understanding of the problem can be gained by studying the aerodynamic forces acting on the plate. The steady aerodynamic force measurement of the blunt flat plate with solid and porous trailing-edges are presented and explained in this subsection. The experiments covered a wide range of flow velocities, U_∞=6 m/s to U_∞=26 m/s, corresponding to the Reynolds numbers of $Re_{L_x} = 1.3{\cdot}10^5$ to $5.8{\cdot}10^5$. The results presented in Fig. 3 show the drag coefficient (C_D) of the plate against the Reynolds number for the solid and porous trailing-edges. The aerodynamic force of the drag coefficient is calculated as $C_D = F_D/$ 0.5 $\rho\ U_\infty^2$ A, where C_D is the drag coefficient, F_D is the stream drag force and A is the plate's plan view area.

Results have shown that the use of porous treatment can significantly reduce the drag force. The results for the baseline (solid) case have shown that the drag coefficient experiences a sudden sharp drop at low Re_{L_x} and gradually reaches an area of almost Re_{L_x} independency at higher Reynolds numbers. It can also be seen that the use of 25 PPI porous material leads to the largest reduction in C_D, roughly 16 % followed by porous media with 80 PPI porosity compared to the solid case. Also, the trend shown by the solid and porous with 80 PPI cases were almost identical at high Reynolds numbers, indicating that the flow at high Reynolds numbers behaves similarly in the case of 80 PPI and solid trailing-edges. This behaviour can be explained by the fact that it takes more space/time for the flow to penetrate into the 80 PPI material,

and therefore the porous material with high PPI and lower permeability behaves more similar to the solid case. The significant reduction obtained for the case of 25 PPI can be attributed to the changes to the flow acceleration and the suppression of the vortex shedding from the TE. These will be further discussed in the following sections.

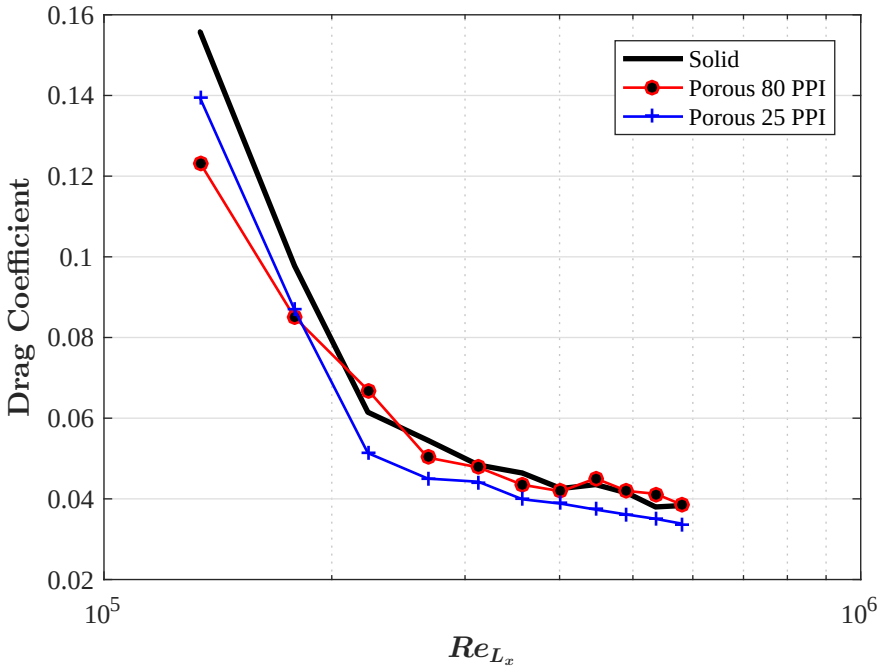

Figure 3: The measured drag coefficients for the different cases: *black line: solid; red line: porous 80 PPI; blue line: porous 25 PPI.*

B. Trailing-edge Flow Field

In order to better understand the effects of the porous trailing-edge on the vortex structures, boundary layer behaviour and the wake velocity profile, measurements have been performed using PIV and hot-wire probes at the flow velocity of U_∞=20 m/s, corresponding to the Reynolds number of $Re_{L_x} = 4.6 \cdot 10^5$. Figure 4 illustrates the time-averaged normalized streamwise (U) and spanwise (V) velocity components for the blunt trailing-edge with and without porous treatment. Results in Figs. 4(a) and 4(b) show that the flow recirculation behind the solid trailing-edge occurs within $0.1 \lesssim x/h \lesssim 0.7$. A small shift of the recirculation region for the case of porous 80 PPI can be seen in Figs. 4(c) and 4(d) where the recirculation occur within $0.2 \lesssim x/h \lesssim 0.8$. Interestingly, the use of porous 25 PPI results in moving the main circulation area to further downstream. This can be seen in Figs. 4(e) and 4(f) where the circulation areas have moved further downstream to $0.5 \lesssim x/h \lesssim 1.3$. Based on the PIV measurements, the vortex formation length (L_f), defined as the distance at the plate trailing-edge to the end of the vortex region, have been found. The L_f/h values for solid, porous 80 PPI and porous 25 PPI trailing-edges are approximately 0.82, 0.84 and 1.3, respectively, indicating a significant delay in the formation of vortex shedding due to interaction of flow with the porous treatment. Another interesting feature acquired from Fig. 4 is that a high acceleration zone appears with maximum streamwise U-velocity (U/U_∞=1.1) upstream of the solid blunt trailing-edge (Fig. 4(a)) and also an immediate overshoot can be seen in the near wake location of the trailing-edge. Similar observation can be seen in the case of porous 80 PPI (Fig. 4(c)) with velocity acceleration lesser than that of solid. Unlike the solid trailing-edge, porous 25 PPI exhibits a much lesser acceleration upstream of the trailing-edge and reduced the overshoot near the blunt trailing-edge significantly. Note that, the acceleration region of the V-components for porous 25 PPI in the wake have moved even further downstream compared to the solid and 80 PPI cases, which suggests that the acceleration is induced by strong vertical V-velocity components in the vortex shedding behind the trailing-edge.

Figure 6 presents the mean and root-mean-square (rms) boundary layer velocity profiles along the BL lines shown in Fig. 5. The measurement is conducted at the flow velocity of U_∞=20 m/s using single hot-wire probes and the data has been collected between $y \approx 0$ mm and $y = 50$ mm at 35 points above the plate for each line. The y-axis of the boundary layer profile have been normalized by the boundary layer thickness at BL_1, x/h=-2.6, upstream of the exchangeable trailing-edge part. Note that at BL_1, the flow velocity approaches to zero at the solid surface, *i.e.* the no-slip condition, which will not be the case over the porous surface due to the flow penetration into the porous medium. The velocity profile results show that there is an increase in the velocity gradient at the wall from BL_1 to BL_4 and the boundary layer thickness found to be decreasing from BL_2 to BL_4. This implies that favorable pressure gradient occurs near the trailing-edge which tend to cause strong flow acceleration over the trailing-edge.[53] All of the boundary layer profile downstream from BL_1 change for all cases, as the bluntness causes significant velocity overshoot in the vicinity of the trailing-edge. The results obtained for the flat blunt plate with porous treatment, however, show that the flow experiences a much less acceleration and overshoot near the trailing-edge, where these observations are in good agreement with the flow velocity streamline results illustrated in Fig. 4. Similarly, this can be interpreted to be due to the pressure drop balance across the porous treatment and penetration of flow into the porous section. The rms velocity results clearly show that the use of porous treatment reduces the velocity rms value over a large part of the boundary layer, particularly in the outer regions. This becomes clearly visible at x/h=-0.9 (BL_3) and x/h=-0.05 (BL_4), upstream of the trailing-edge, where the flow acceleration had been observed. However, there is an increase in the rms velocity magnitude near the wall region, especially for the case of porous 25 PPI at both BL_3 and BL_4. The increase in the energy content of the velocity fluctuations in the vicinity of the porous surface can be attributed to frictional forces acting at the rough surface of the porous material. However, results show that the overall energy content in the boundary layer is significantly reduced by both porous materials. This is particularly an interesting result as it shows that the energy content of the large coherent structures in the log-law and outer layer regions, mainly responsible for the surface pressure fluctuations and the trailing-edge noise generation,[49] can be significantly reduced using porous treatments.

Figure 7 shows the streamwise (U) and vertical (V) velocity profiles at different axial locations, namely x/h= 0.1, 0.5, 1.0, 2.0, 3.0, and 5.0 downstream of the trailing-edge (see Fig. 5), covering a wide range of near-wake and far-wake locations to properly capture the wake behaviour. It is clearly visible that the porous treatment can significantly change the wake profiles in the near wake region. Results show that the 25 PPI material significantly reduces the magnitude of the streamwise velocity in the wake, while the 80 PPI is closer to the solid case, but still gives a reasonable reduction. The U velocity profiles show that the porous treatment delays the formation of vortex shedding in the wake, *i.e.* near-wake stabilization which is consistent with the streamline topology in Fig. 4. It can be generally seen that the momentum deficit in the porous cases especially for the case of porous 25 PPI is larger than that of the solid case at all downstream locations. The modest deficit in the case of solid trailing-edge is due to the existence of strong U and V flow velocity components in the near-wake because of the recirculation region at the trailing-edge and the velocity overshoot, which leads to vortex shedding near the trailing-edge. On the other hand, the strongest deficit observed in the case of 25 PPI is due to suppression of the recirculation region and reduction of the velocity overshoot at the trailing-edge, resulting in a more streamlined flow over the trailing-edge and larger deficit in the plate near-wake region. The difference between the solid and porous trailing-edge results decreases at downstream locations. The porous material restraint the entrainment of the high momentum fluid from the free-stream into the wake field, which causes lower momentum transfer in the wake and results in large velocity deficit in the case of porous trailing-edge. Also, the results observed for the higher streamwise mean velocity in the region of $0.5 < y/h < 2$, indicates that the porous trailing-edges, especially for the 25 PPI case have smaller drag forces than the solid trailing-edge. Lim *et al.*[54] showed that the large velocity deficit in the wake region promotes lower drag force in the case of bluff bodies. This evidence is in agreement with the results obtained in Fig. 3. The V-velocity component results show a different behaviour than the U-velocity component. The vertical velocity component in the near-wake can be linked to the vortex formation and rolls-up mechanism. The V-velocity results for the solid trailing-edge at $x/h = 0.1$ shows the existence of a secondary small recirculation area near the center-line ($y = 0$) and two larger recirculation area nearer to the trailing-edge. The small recirculation near the centreline disappears quickly further downstream, leading to only only large recirculation areas, ending between $x/h = 2.0$ to 3.0. The V-component observed for the 80 PPI trailing-edge is very similar to that of the solid trailing-edge, but the 25 PPI trailing-edge exhibits a very different behaviour. The recirculation area in the near-wake of the 25 PPI trailing-edge is much

larger than that of the solid TE and stretches to almost $x/h = 1.0$. The main recirculation area near the trailing-edge, on the other hand, is much weaker than the solid case, indicating the stabilization of the shear layer and delay of the vortex shedding formation which generally matches with the PIV results, depicted in Fig. 4. This will be further discussed in Figs. 8 and 10.

Figure 8 presents the Reynolds normal stress ($\overline{u'u'}/U_\infty^2$, $\overline{v'v'}/U_\infty^2$) and the eddy shearing stress ($-\overline{u'v'}/U_\infty^2$) components within the wake at x/h= 0.1, 0.5, 1.0, 2.0, 3.0, and 5.0. It is clear from the figure that the Reynolds stresses are symmetrical about the wake center-line for all cases and peak at about the trailing-edge location $y/h = \pm 0.5$. The near-wake results show that the use of porous trailing-edge can lead to significant reduction of the normal and shear stress along the centre-line, to almost zero, and also considerable reduction at the peak location ($y/h = \pm 0.5$). It can, therefore, be concluded that the effect of porous treatment on the trailing-edge was to break-down the large flow structure in the near wake which was signified by the reduction in the velocity fluctuations in the wake region particularly for the case of porous 25 PPI. Results show that the use of porous trailing-edge leads to considerable reduction of the wake width in the y-direction at $x/h = 3.0$ and 5.0. Results have also shown a noticeable difference between the magnitude of the $\overline{u'u'}$ and $\overline{v'v'}$ normal stress terms. The results obtained for the solid and porous trailing-edges show that the $\overline{v'v'}$ becomes twice as large as the $\overline{u'u'}$, or more, at the downstream locations. The increase in the v-fluctuations indicates the presence of large swirling turbulent structures, *i.e.* the formation of vortex shedding.[55] Also, this suggests the existence of a highly anisotropic flow at these locations due to the vortex formation. The energy production by the Reynolds shear stress is the primary mechanism for the destabilization of the Tollmien–Schlichting instability. It is, therefore, also important to study the Reynolds shear stress component ($-\overline{u'v'}/U_\infty^2$). The results at each location display a symmetrical distribution of shear stress along the wake center-line. The region with strong local production of turbulence can be seen in the case of solid trailing-edge in the near wake, which its shear stress gradient is larger relative to the porous cases. It is clear that the shear stress is reduced significantly at x/h=0.1 to x/h=2.0 due to the larger momentum deficit in the case of 25 PPI. Also, the lower peaks in the case of 25 PPI compared to the solid trailing-edge is due to the elongation of the wake region and the suppression of vortex shedding. In contrast, the distribution of $-\overline{u'v'}$ obtained at x/h=3.0 and x/h=5.0 shows a slight increase in the peak concentration in the porous 25 PPI case. It is also clear that the fluctuations of the velocity components have negligible values in the porous 80 PPI case at the last two locations indicating that the vortices are removed.

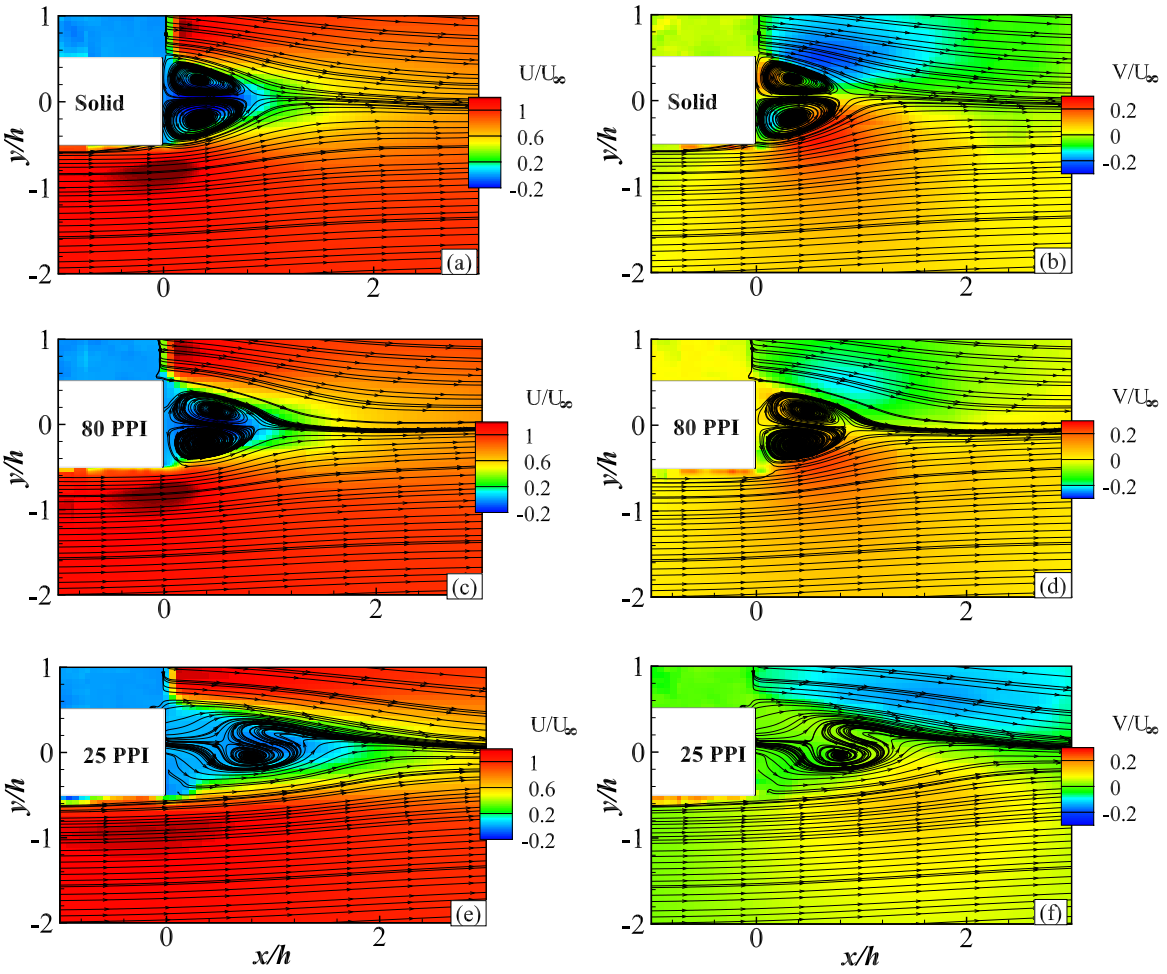

Figure 4: Time-averaged streamline topology for normalized U velocity components ((a) solid TE, (c) porous 25 PPI TE, (e) porous 80 PPI TE) and normalized V velocity components ((b) solid TE, (d) porous 25 PPI TE, (f) porous 80 PPI TE), at U_∞=20 m/s

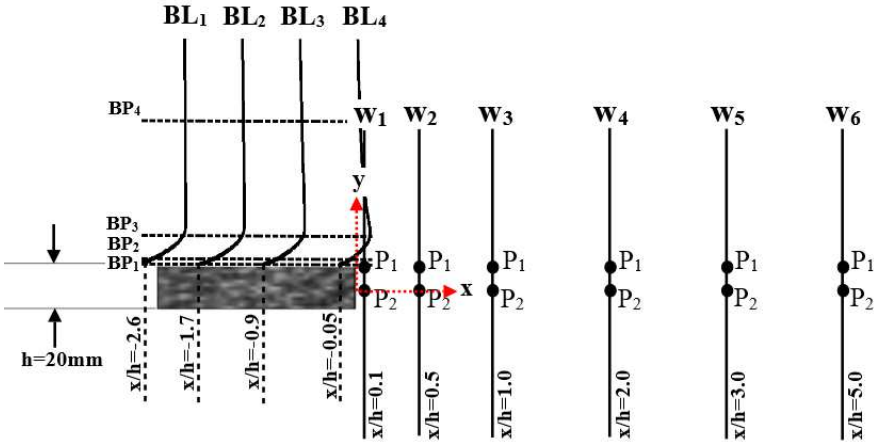

Figure 5: The schematic of the blunt trailing-edge rig and the positions of the hot-wire measurements

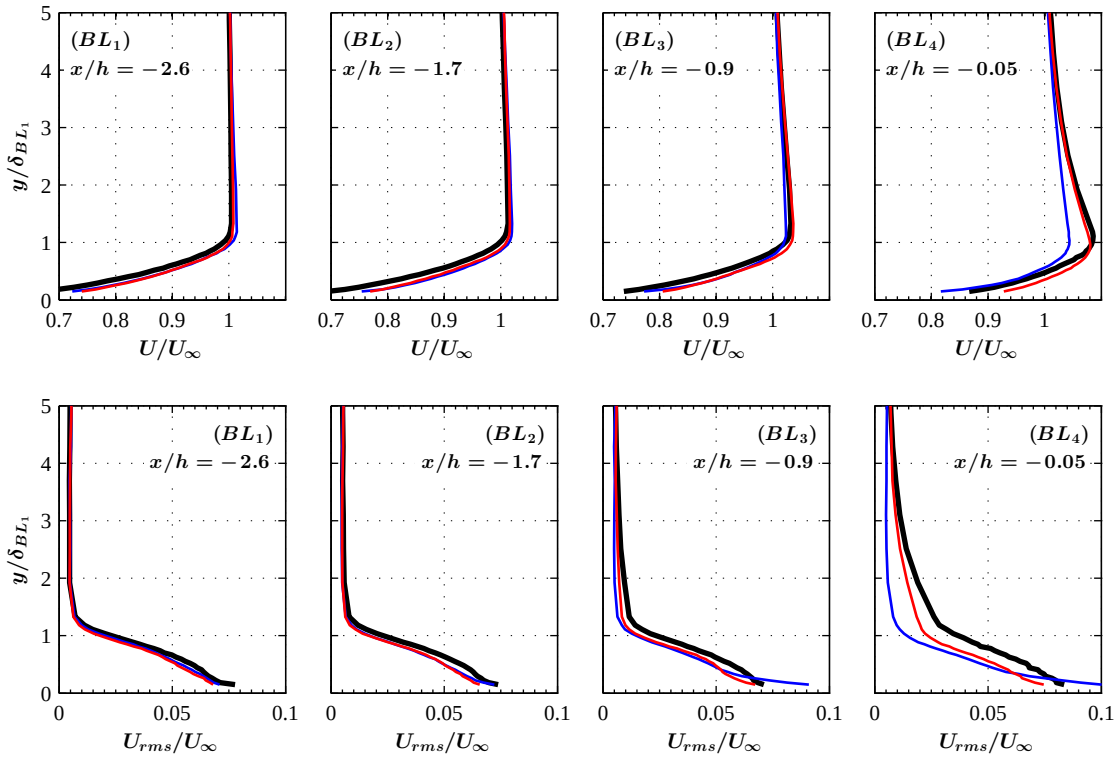

Figure 6: Boundary layer mean and RMS velocity profiles at different streamwise locations over the blunt trailing-edge flat plate model. *black line: solid; red line: porous 80 PPI; blue line: porous 25 PPI.*

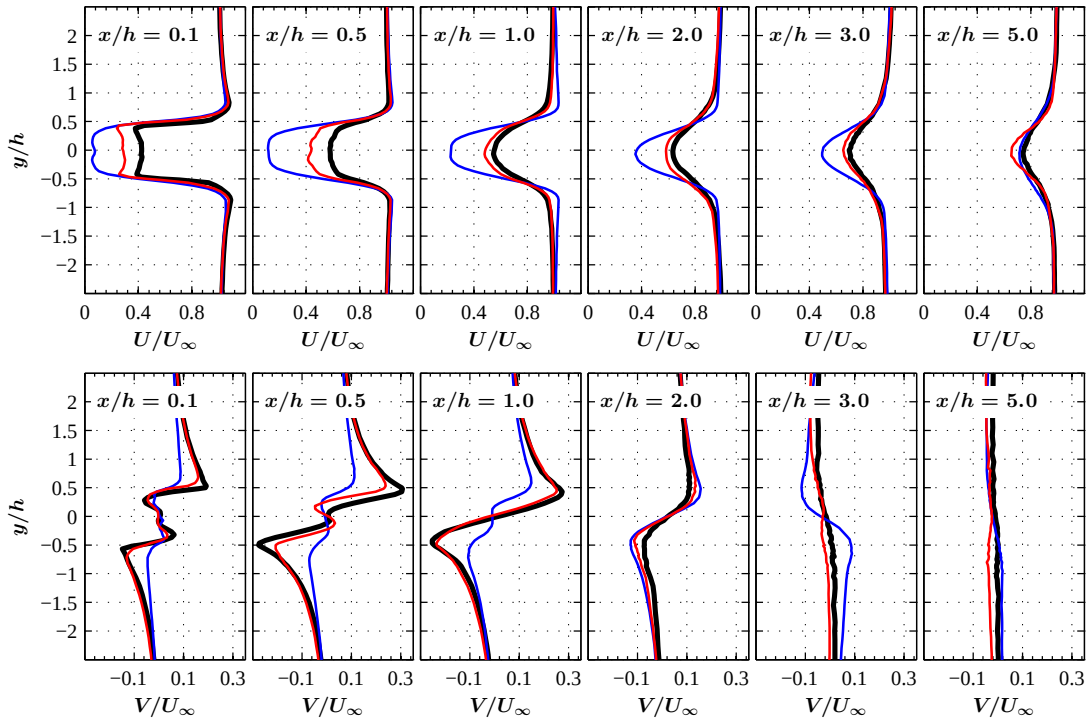

Figure 7: Mean U and V velocity components in the wake of the blunt trailing-edge. *Black line: Solid; Red line: Porous 80 PPI; Blue line: Porous 25 PPI.*

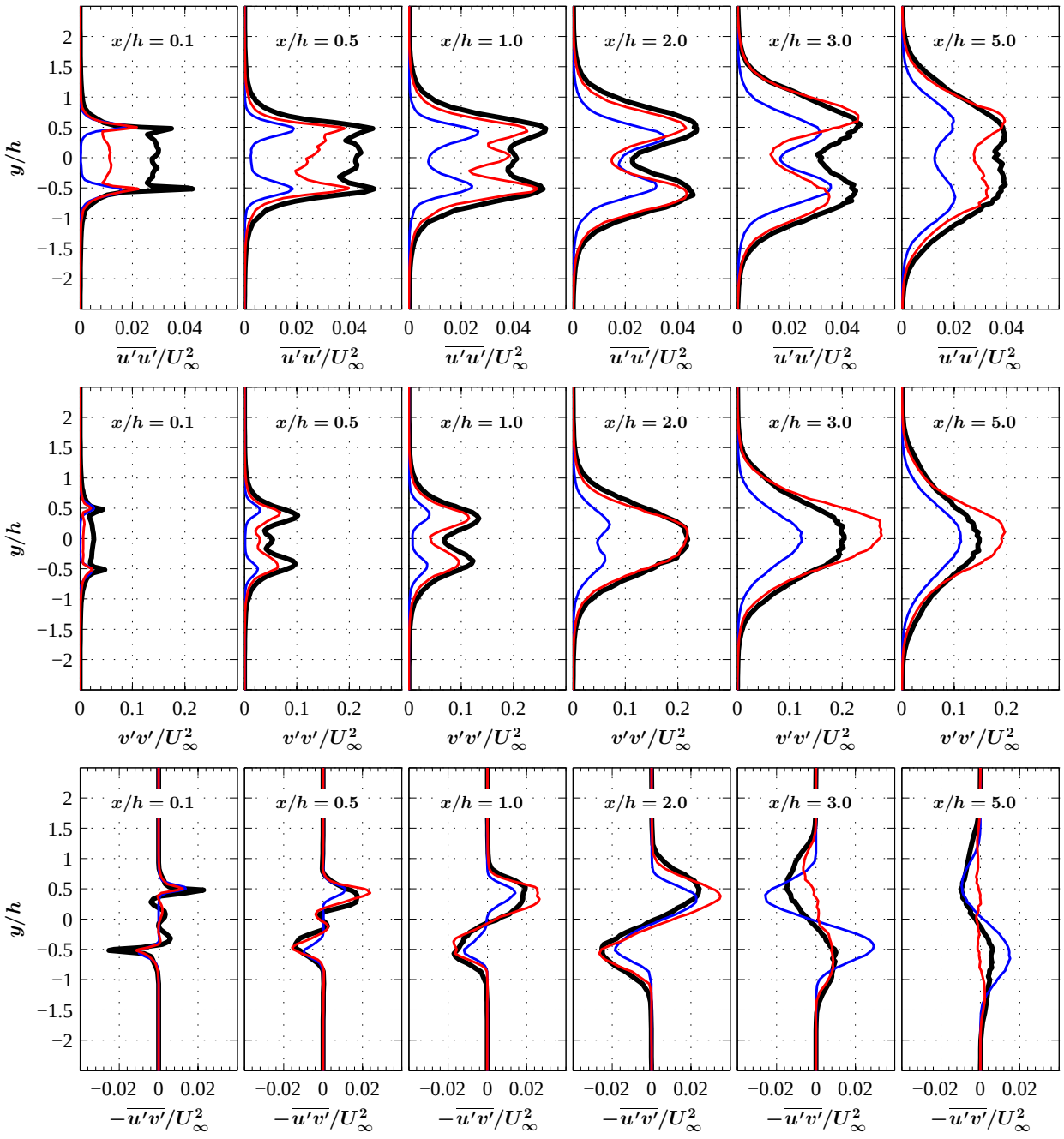

Figure 8: Reynolds stress components within the wake. *Black line: Solid Red line: Porous 80 PPI; Blue line: Porous 25 PPI.*

C. Velocity Power Spectra in the Boundary Layer and Wake

The dominant turbulent structures within the boundary layer and their frequency-energy content can be studied using the velocity power spectrum (ϕ_{uu}). Figure 9 presents the velocity power spectral density (PSD) as a function of the Strouhal number (St=$fh/\ U_\infty$) at different axial locations upstream of the trailing-edge and provides a comparison between the three investigated trailing-edge cases. In order to estimate the energy content at different frequencies, the Welch's power spectral density of velocity fluctuations (ϕ_{uu}) has been performed based on the time-domain hot-wire data using Hamming windowing for segments of equal length with 50 % overlap. The frequency resolution (Δf) was set to 64 Hz and the frequency wavelength was equal to 1/5 of the window length used in the windowing process. The velocity fluctuation energy spectra results at BP_1 correspond to the point near the surface (y=0.5 mm), while BP_{2-3}, *i.e.* the top two rows, show the results further away from the wall regions of the boundary layer. Due to the complexity of the near-the-wall flow and difficulties in the measurement of the friction velocity u_τ for the porous surface, it is rather difficult to accurately determine the boundary layer regions. Results have shown that in the vicinity of the wall the porous material especially in the case of 25 PPI causes an increase in the energy content over the whole Strouhal range which is believed to be due to the increased level of frictional forces acting on the fluid near the surface, which is also in agreement with the rms velocity results presented in Fig. 6. It can also be seen that the level of such frictional forces increases with the fluid travelling downstream over the porous section. The investigated spectra at BP_3, BL_{2-4} clearly show that the energy content of the boundary layer structures reduced significantly as a result of the boundary layer interaction with the porous surface. The results for the solid trailing-edge also show a strong tonal behaviour at $St \approx 0.21$, which can be attributed to either the wake vortex-shedding energy back-scattered over the trailing-edge area or the presence of hydrodynamic field over the trailing-edge section. This will be further discussed in subsection D. This tonal peak energy has been detected in almost all locations, which are also visible in the case of porous 80 PPI shown in Fig. 9, except for regions far upstream of the trailing-edge and very close to the surface. Interestingly, in the vicinity of the trailing-edge at BL_{3-4} results show that the use of 25 PPI porous material results in the complete suppression of the tonal peak and the emergence of a small broadband peak between St = 0.3 to 0.9 at BP_3, BL_4. This phenomenon can also be seen in the near wake energy content and the surface pressure level results in Figs. 10 and 11. One can infer from the results that the two porous materials have very different effects on the tonal peaks, as well as the broadband energy content of the turbulent structures with the boundary layer upstream of the trailing-edge. From the velocity PSD results presented in Fig. 9, one can conclude that the use of porous material can lead to significant reduction of the energy content of the large turbulent structures within the boundary layer and the suppression of the vortex shedding tonal peaks. Understanding of the mechanisms through which the porous treatment causes such changes, requires more in-depth analysis of the boundary layer surface pressure fluctuations, which will be dealt with in subsection D.

In addition to the mean velocity and Reynolds stress components shown in Figs. 7 and 8, to properly understand the turbulence structures within the wake region, it is important to study the energy-frequency content of the wake structures at different locations. The power spectral density of the streamwise velocity (ϕ_{uu}) are presented at several wake locations downstream of the trailing-edge lip-line and along the center-line, see Fig. 10. The measurement locations are shown in Fig. 5. The fundamental, first and second harmonics of the vortex shedding frequency can be clearly seen from the results of the solid trailing-edge along the trailing-edge and center-line. Results show a significant and consistent reduction of the ϕ_{uu} in the case of porous 25 PPI along the center-line, as expected from the $\overline{u'u'}/U_\infty^2$ results. A broadband peak region is obvious at about $0.3 < St < 1.0$ for porous 25 PPI and $0.5 < St < 2.0$ for porous 80 PPI in the near-wake region (P_1, W_1), which was also observed in the boundary layer power spectra (Fig. 9(BL_4)) results. This broadband peak is, however, local to the trailing-edge region, dissipates very quickly further downstream and is believed to be due to the local hydrodynamic properties such as, the effects of permeability between the porous 25 PPI medium and the flow, which will be further discussed in subsection D. The results further downstream and along the trailing-edge lip-line ($y/h = 0.5$) have shown that the use of porous trailing-edge can result in significant reduction of the broadband energy content of the turbulent structures up to 5 dB. The results along the center-line ($y/h = 0$), on the other hand, have shown very strong reduction of ϕ_{uu} over the entire frequency range, particularly within the near-wake region ($x/h < 2$). The presence of the vortex shedding is distinctly pronounced with the appearance of several tonal peak values in the spectra. The amplitude of these peaks are reduced by both porous materials, and the 25 PPI treatment also nearly eliminates the peaks in the early wake. A possible reason is that the fluid loses its energy due to the strong

dissipation of flow penetrating into the porous surface. However, the tonal structures in the 25 PPI case increases at downstream locations (x/h = 1.0 and 2.0) and significant reduction of the peak magnitude and the broadband energy content can be seen at (x/h = 5.0). In the upper plots, the similar peaks and its harmonics (at St=0.2 and St=0.4) can be seen for the porous 80 PPI case, whose peaks reach that of the baseline (solid) values at the farther downstream locations. The spectra velocity gradient shown in the plots appears close to the slope with $f^{-5/3}$ in the downstream locations for all cases, where the high turbulence kinetic energy occur. The spectra slope subsequently increases at higher frequencies.

D. Boundary Layer Dynamic Surface Pressure

In order to better understand the effects of the porous surface, the statistical features of the boundary layer, such as the surface pressure fluctuations, lateral coherence of the turbulence structures and the velocity-pressure coherence over the blunt trailing-edge have been investigated.

1. Wall Pressure Power Spectra

The power spectral density of the surface-pressure fluctuations (ϕ_{pp}) obtained from the pressure transducers *p1*, *p2*, *p4* and *p6* are presented in Fig. 11. The vortex shedding peak can be seen at $St \approx 0.21$ at all transducer locations for the solid case, and the peak is slightly shifted to higher St number in the case of porous 80 PPI. Similar to the result obtained in Fig. 9, no tonal peak is seen for the case of porous 25 PPI, which again confirms that the vortex shedding has been effectively eliminated by the porous treatment. The tonal peak for the case of solid protrudes more than twice above the broadband energy content while that for porous 80 PPI is in the order of 0.5 to 1.5, and almost negligible for porous 25 PPI. Result have also shown that the porous treatment can increase the broadband energy content in the whole frequency ranges due to the frictional forces effect exhibited by the porous structure. Results for the 25 PPI case also show the development of broadband peak structure at $St \approx 0.5$, in addition to the general increase in pressure fluctuations at higher Strouhal numbers, which is consistent with the findings illustrated in Figs. 9 (BP_{1-3}, BL_4) and 10. Similar observation can be made from the numerical analysis conducted by Das *et al.*,[56] where significant broadband peak was visible in the velocity and pressure for materials with high permeability constant.

It is worth emphasizing again that both of the porous 25 and 80 PPI materials exhibit a large rise in pressure and velocity (Fig. 6) fluctuations at the surface compared to that of solid, which are associated with the frictional forces acting at the rough surface of the porous materials. However, the roughness alone does not seem to be the sole reason for the existence of the broadband peak, which only appears for the 25 PPI material and it is therefore, important to take a closer look at other important parameters, such as the porosity and permeability. Hence, to better understand this phenomena, a comprehensive study have been conducted to analyze the effect of roughness and permeability on the surface pressure fluctuations of the 25 PPI material. The effects of roughness attendant to the porous surface and permeability have been examined independently and together by filling the porous 25 PPI trailing-edge with different sand heights namely, 50%, 75%, 90%, and 100% filled, relative to the porous section thickness (h=20 mm). In order to ensure there is no leakage of flow through the sand-porous medium and also to avoid sand leaving the porous section during the wind tests, the sand is slightly dampened and kept within the material's open pores. Results in Fig. 12 show clearly that the emergence of broadband peak at $St \approx 0.5$ only can be seen for the configurations with the lowest sand ratio (50 %) and without the sand. It can also be observed that the broadband peak gradually disappears as the amount of sand height in the porous increases. The results obtained for the porous with full sand configuration are almost similar, with slightly lower ϕ_{pp}, to that of the solid case (Fig. 11). Furthermore, the peaks magnitude reduces with increasing permeability and similar to the observation beforehand, the peak is completely eliminated with the porous configuration without sand. The findings here clarify that the appearance of the localized broadband peak at a certain frequency regions are mainly associated with porous material with larger permeable conditions. This can also be related to the velocity slippage at the porous surface within the boundary layer, which may cause a well-established hydrodynamic field and flow circulation inside the porous structure. However, the possible reasons on how such phenomena occur has been difficult to determine experimentally. Despite its complexity, the numerical analysis of porous flow by Das *et al.*[56] has shed light upon understanding of the flow regimes within the porous medium using a finite volume model in three-dimensions. They found the existence of flow circulation inside the porous medium with high permeability and it was shown that the flow can be in a reverse direction

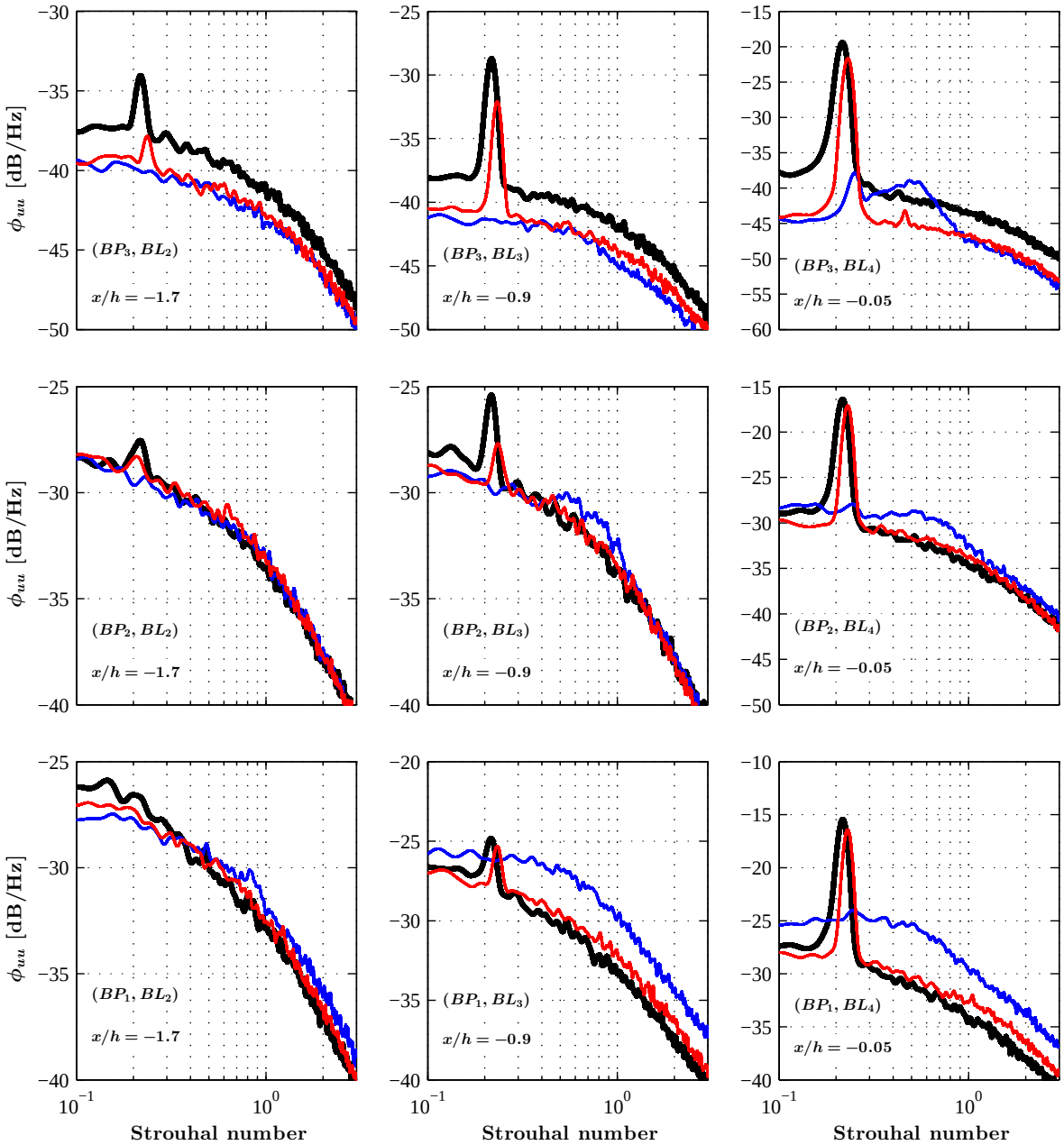

Figure 9: The power spectral density at different locations in the boundary layer. *black line: solid; red line: porous 80 PPI; blue line: porous 25 PPI.*

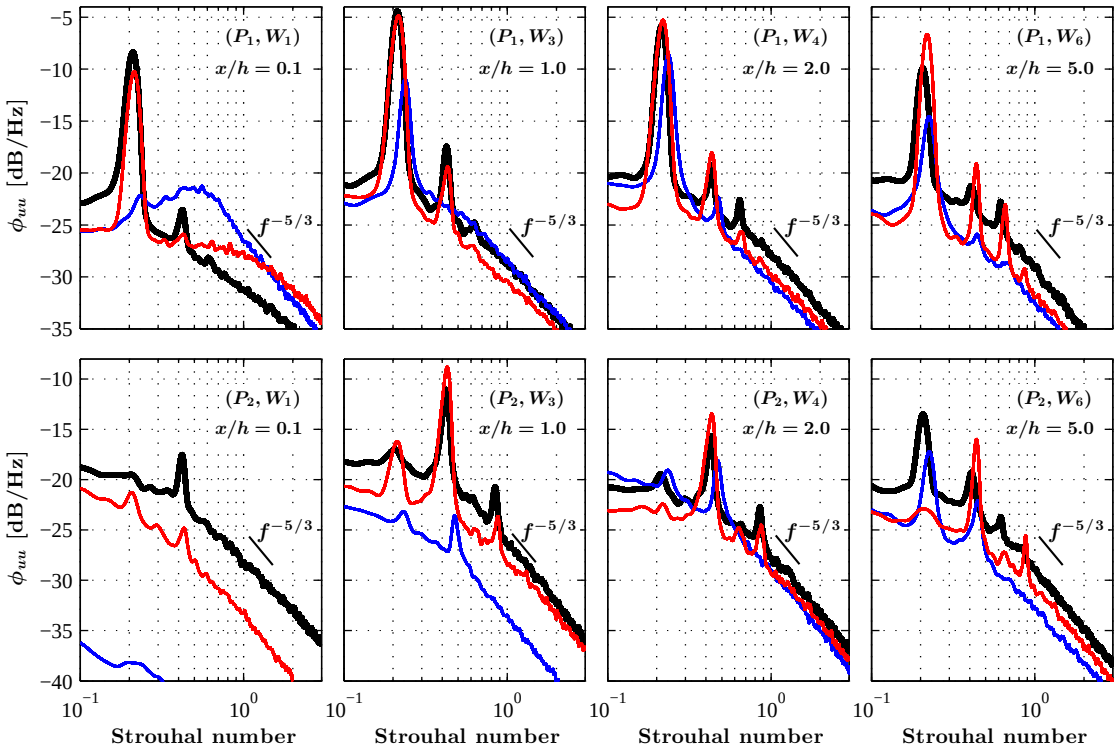

Figure 10: The power spectral density of the streamwise velocity at different locations in the wake. *Black line: Solid; Red line: Porous 80 PPI; Blue line: Porous 25 PPI.*

at the interface between the porous region and the flow. It has also been reported that the flow circulation in the porous medium disappears after a time interval. Hence, it is envisaged that the evolution of the broadband peak in the present study is believed to be associated with the presence of flow circulation inside the porous medium, however, more investigations are required to provide a robust hydrodynamic analysis within the porous domain.

2. Boundary layer Lateral Coherence and Velocity-Pressure Coherence

The spatial coherence of the turbulent structures between two stationary signals in the time domain between the spanwise transducers and between the velocity and surface pressure signals can be evaluated using the coherence functions given by Eqs. 1 and 2 as,

$$\gamma^2(f, \Delta z) = \frac{|\Phi(f, z_1, z_2)|^2}{|\Phi(f, z_1, z_1)||\Phi(f, z_2, z_2)|}, \tag{1}$$

and

$$\gamma^2(f, \xi y) = \frac{|\Phi(f, p_i, u_i)|^2}{|\Phi(f, p_i, p_i)||\Phi(f, u_i, u_i)|}, \tag{2}$$

where $\Phi(f, z_1, z_2)$ denotes the cross-power spectral density function between two pressure signals, Δz is the spatial separation along the z-direction and f is the frequency. $\Phi(f, p_1, u_2)$ denotes the cross-power spectral density function between two velocity and pressure signals, ξ_y is the distance between measurement locations normal to the plate (y) direction. The y-axis of the velocity-pressure coherence plots have been normalized by the boundary layer thickness at BL_1 (Fig. 5).

Figure 13 illustrates the lateral coherence measured between the spanwise transducers *p2*, *p7*, *p8*, *p9*, *p10* and *p11* at x/h=-0.7. The left column figures (a, c and e) show the coherence of five spanwise distances between the selected transducers while the right column figures (b, d and f) show the coherence of all 15

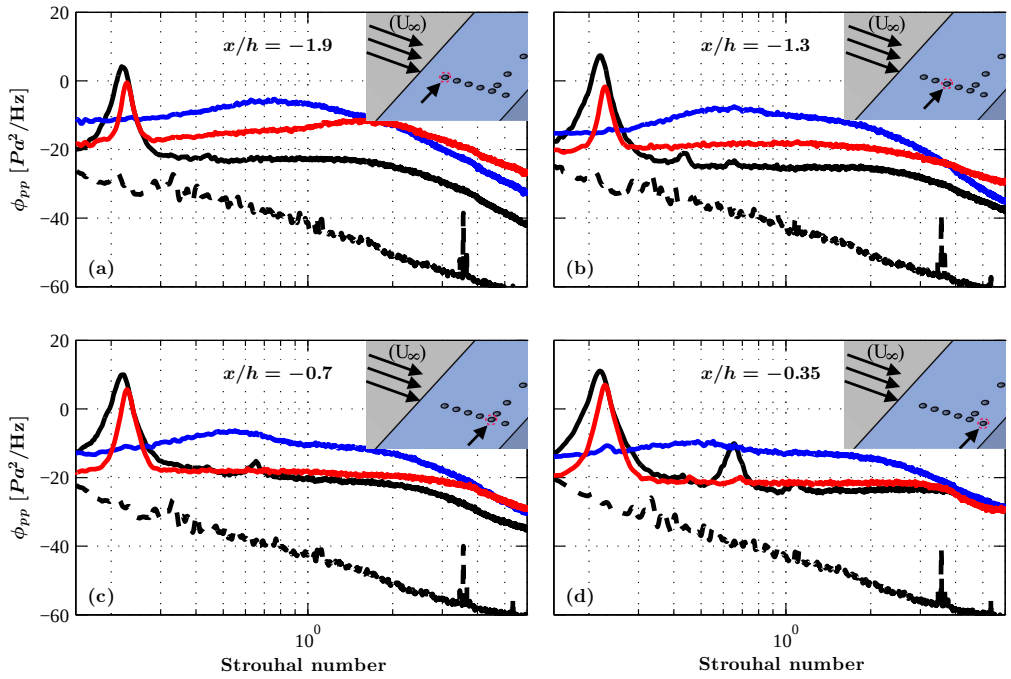

Figure 11: Power spectral density of pressure measured by transducers, (a) *p6* (x/h=-1.9), (b) *p4* (x/h=-1.3), (c) *p2* (x/h=-0.7), (d) *p1* (x/h=-0.35). *dashed black line: background noise; black line: solid; red line: porous 80 PPI; blue line: porous 25 PPI.*

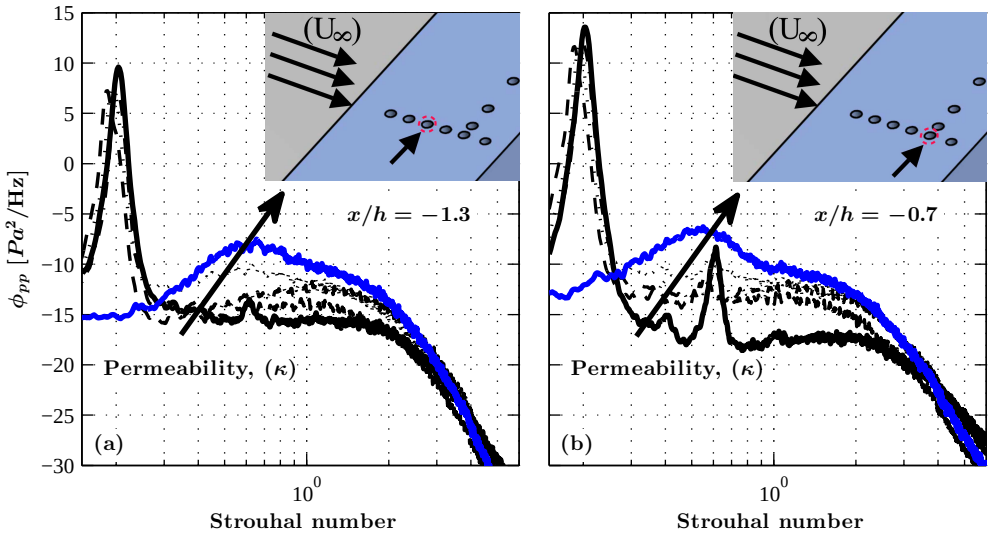

Figure 12: Power spectral density of pressure measured by transducers *p4* (x/h=-1.3) and *p2* (x/h=-0.7) with different permeability configurations. *Full Sand (———); 0.90 Sand (- - - - -); 0.75 Sand (-·-·-·-); 0.50 Sand (·····); No Sand (———).*

combinations of the spanwise distances between all the six transducers. The figures are plotted as a function of the Strouhal number (fh/U_∞). The results clearly show that the porous treatments have major and different effects on the lateral coherence of the flow structures, depending on the mechanical properties of the porous material. As expected, there is a strong high coherence between the pressure fluctuations for the case of solid, whereas much lower coherence values can be seen in the case of the 25 PPI material. Results have also shown that at the vortex shedding frequency, $St \approx 0.21$, for both the solid and 80 PPI material, a strong coherence can be observed, while for the 25 PPI material, the lateral coherence at the vortex shedding peak has been significantly reduced. Also, it is seen that the coherence of the pressure fluctuations become stronger at $St \approx 0.7$ for the case of solid. The lateral coherence of the turbulent structure has been completely eliminated at $St > 1$ as the eddies became independent of each other. It is noticed that the porous 80 PPI exhibits higher coherence at the tonal peaks, and, at the same time, eliminates the broadband frequency coherence content. On the contrary, the 25 PPI material eliminated the vortex shedding peak completely, however similar to the finding beforehand, it is clear that a broadband peak has emerged at the same Strouhal number of $St \approx 0.5$. From these results, it is clear that the 80 PPI material is able to notably eliminate the broadband energy content whereas the 25 PPI material can effectively eliminate the vortex shedding tonal peaks.

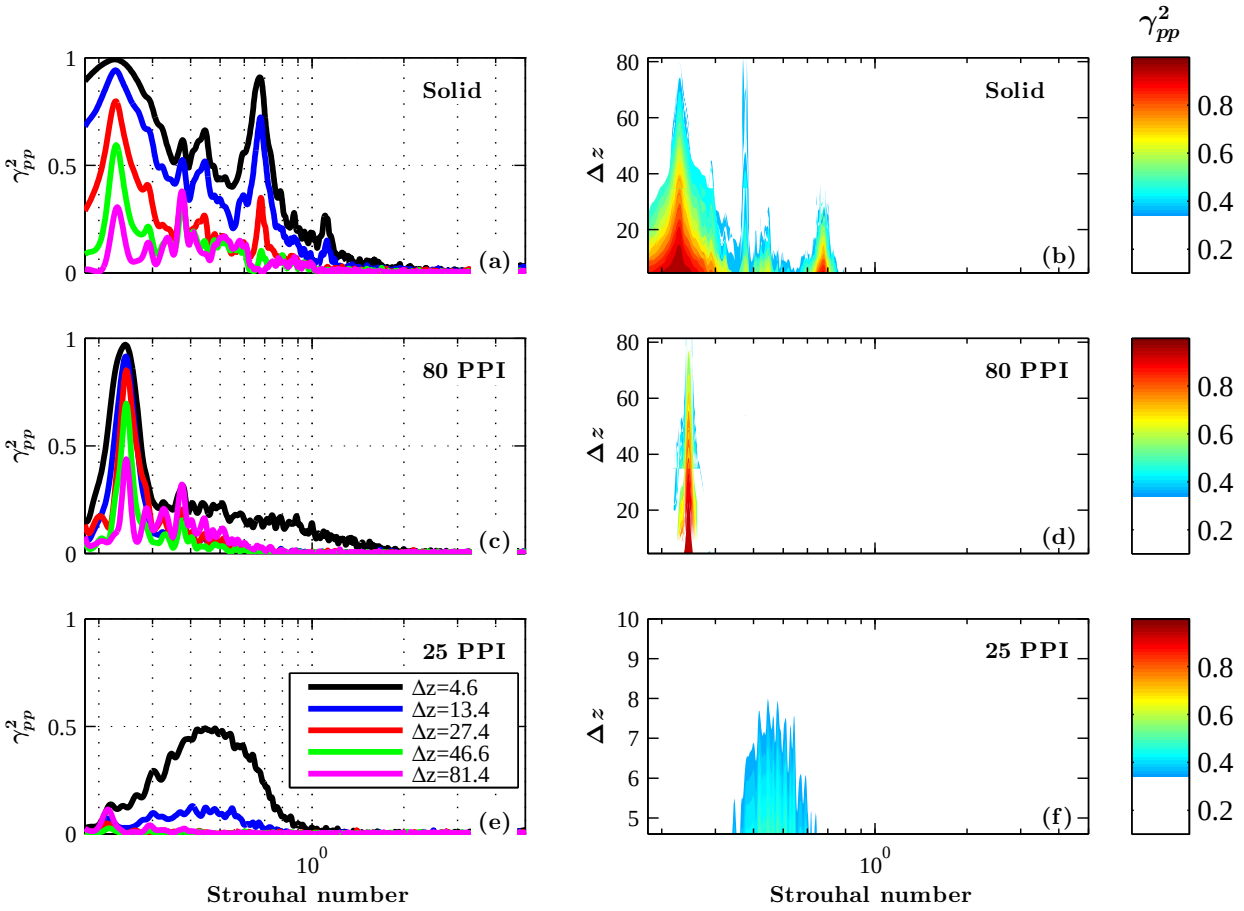

Figure 13: Lateral coherence between spanwise transducers at x/h=-0.7

Figure 14 shows the coherence between the velocity and surface pressure signals at *p1*, (x/h=-0.35), corresponding to the main region where strong flow acceleration occurs, see Figs. 4 and 6 (BL_4). The left and right columns in Fig. 14 show the coherence of the u- and v-components of the flow velocity with the pressure signal (γ^2_{up}, γ^2_{vp}), respectively. The figure demonstrates that a strong coherence can be seen at the vortex shedding frequency, $St \approx 0.21$ for the case of solid trailing-edge and porous 80 PPI. In contrast, a weaker coherence can be seen at the vortex shedding frequency for the case of porous 25 PPI, which is

consistent with the small peaks observed in Fig. 11 (x/h=-0.35). Note that, this spectral peak for the case of 25 PPI material is not visible in the near wall of the boundary layer velocity spectra (Fig. 9 (BP_1, BL_4)). However, at the location farther from the surface (BP_3, BL_4) and in the near wake (Fig. 10 (x/h=0.1), the peaks become slightly more visible but strongly attenuated. These findings prove that the two-dimensional vortex shedding structures near the wall in the boundary layer for porous 25 PPI are weak, compared to the strong frictional forces acting on the surface, and therefore not visible. Furthermore, it can also be seen that a small broadband frequency peak appears between St=0.3 to St=0.9, similar to the result obtained in the boundary layer velocity spectra profile presented in Fig. 9 (BP_3, BL_{2-4}) and 11, which is believed to be due to the localized hydrodynamic field and flow circulation inside the porous structure, which only occurs in the case of porous materials with high permeability. The results also show that the coherence between the v-flow velocity with the pressure signals, (γ^2_{vp}) is much more stronger than that of the u-flow velocity with the pressure signals, (γ^2_{up}).

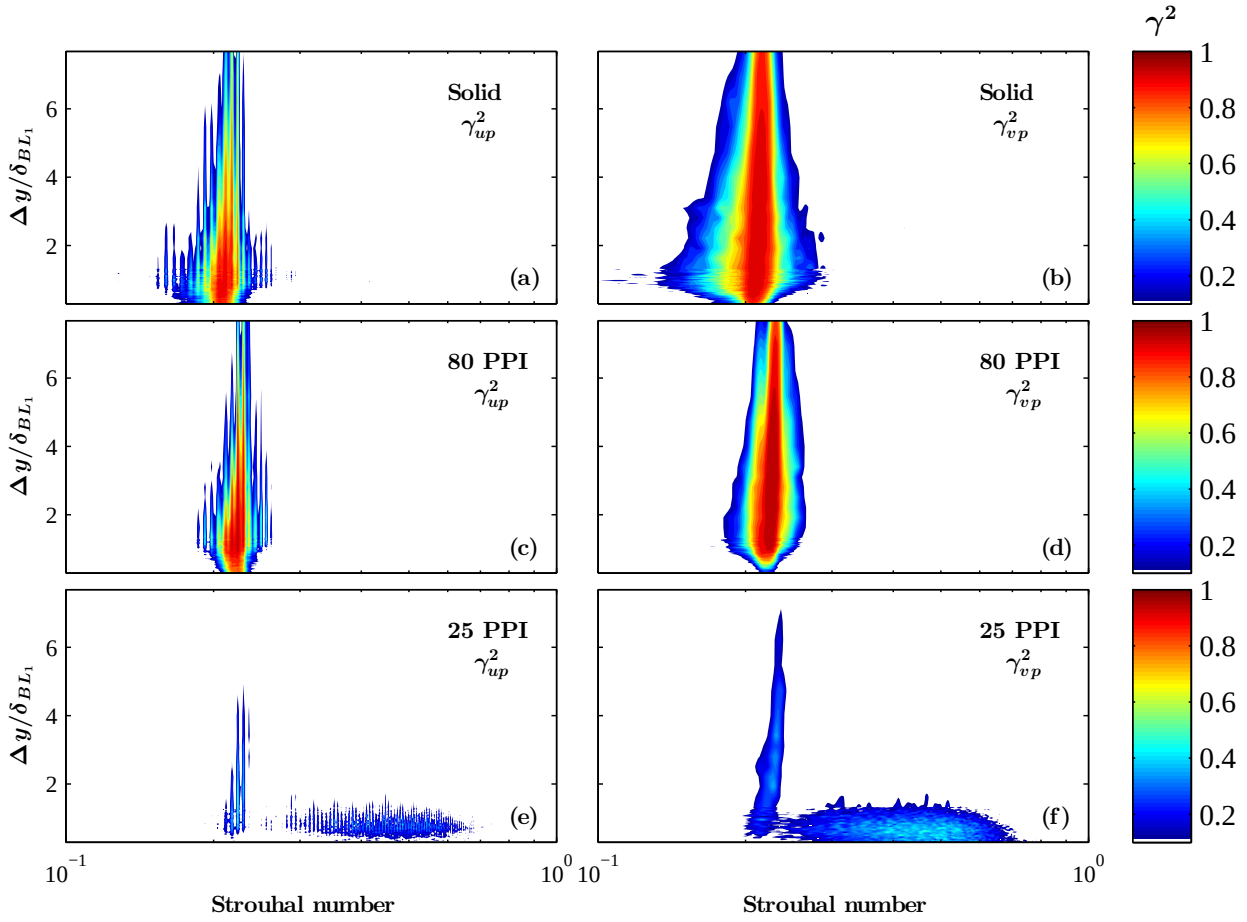

Figure 14: Velocity-pressure coherence, γ^2_{up} (left column) and γ^2_{vp} (right column) in the boundary layer correlation profiles at *p1*, (x/h=-0.35)

IV. Conclusions

The problem of flow around a blunt trailing-edge has been considered in this study. The use of porous materials as a passive method for the control of vortex shedding and noise radiation has been investigated. It has been shown that the 25 PPI material yields to consistent drag reduction for all flow speeds, while the 80 PPI gives less significant drag reduction at high velocities. It is also shown that the porous materials are capable of reducing the acceleration of the flow in the boundary layer upstream of the trailing-edge due to the pressure difference at the blunt trailing-edge. It was found that the porous trailing-edge can delay the vortex

shedding and significantly increase the vortex formation length, leading to a very low turbulent near-wake region. The velocity and pressure power spectral results showed that significant flow energy reduction at the vortex shedding frequency can be achieved with the 80 PPI material and complete suppression of the vortex shedding tonal peak can be seen with the 25 PPI treatment. Furthermore, results have also shown the emergence of small frequency broadband peak in the case of 25 PPI material, which is likely to be due to the localized hydrodynamic field and the existence of flow circulation inside the porous structure, which only appears in the case of porous materials with high permeability. It is also obvious that a noticeable reduction in the lateral coherence of the turbulent structure is seen in the case of porous trailing-edge. One can therefore conclude that the present passive control method using porous media is found to be efficient and promising in controlling the noise generation mechanism and improving the aerodynamic performance.

Acknowledgments

This project is sponsored by Embraer S.A.. The second author (MA) would like to acknowledge the financial support of the Royal Academy of Engineering.

References

[1]Lim, H.-C. and Lee, S.-J., "Flow control of a circular cylinder with O-rings," *Fluid Dynamics Research*, Vol. 35, No. 2, 2004, pp. 107–122.

[2]Bearman, P. and Harvey, J., "Control of circular cylinder flow by the use of dimples," *AIAA journal*, Vol. 31, No. 10, 1993, pp. 1753–1756.

[3]Lim, H.-C. and Lee, S.-J., "Flow control of circular cylinders with longitudinal grooved surfaces," *AIAA journal*, Vol. 40, No. 10, 2002, pp. 2027–2036.

[4]Akilli, H., Sahin, B., and Tumen, N. F., "Suppression of vortex shedding of circular cylinder in shallow water by a splitter plate," *Flow Measurement and Instrumentation*, Vol. 16, No. 4, 2005, pp. 211–219.

[5]Liu, X., Kamliya Jawahar, H., Azarpeyvand, M., and Theunissen, R., "Wake development of airfoils with serrated trailing edges," *22nd AIAA/CEAS Aeroacoustics Conference*, AIAA 2016-2817.

[6]Liu, X., Azarpeyvand, M., and Theunissen, R., "Aerodynamic and Aeroacoustic Performance of Serrated Airfoils," *21st AIAA/CEAS Aeroacoustics Conference*, 2015, p. 2201.

[7]Lyu, B., Azarpeyvand, M., and Sinayoko, S., "Prediction of noise from serrated trailing edges," *Journal of Fluid Mechanics*, Vol. 793, 2016, pp. 556–588.

[8]Lyu, B., Azarpeyvand, M., and Sinayoko, S., "A trailing-edge noise model for serrated edges," *21st AIAA/CEAS Aeroacoustics Conference*, AIAA 2015-2362.

[9]Azarpeyvand, M., Gruber, M., and Joseph, P., "An analytical investigation of trailing edge noise reduction using novel serrations," *19th AIAA/CEAS aeroacoustics conference*, AIAA 2013-2009.

[10]Gruber, M., Azarpeyvand, M., and Joseph, P. F., "Airfoil trailing edge noise reduction by the introduction of sawtooth and slitted trailing edge geometries," *integration*, Vol. 10, 2010, pp. 6.

[11]Gruber, M., Joseph, P., and Azarpeyvand, M., "An experimental investigation of novel trailing edge geometries on airfoil trailing edge noise reduction," *19th AIAA/CEAS Aeroacoustics Conference*, A1AA 2013-2011.

[12]Ai, Q., Azarpeyvand, M., Lachenal, X., and Weaver, P. M., "Aerodynamic and aeroacoustic performance of airfoils with morphing structures," *Wind Energy*, Vol. 19, No. 7, 2016, pp. 1325-1339.

[13]Ai, Q., Weaver, P., and Azarpeyvand, M., "Design optimization of a morphing flap device using variable stiffness materials," *24th AIAA/AHS Adaptive Structures Conference*, AIAA 2016-0816.

[14]Showkat Ali, S. A., Szoke, M., Azarpeyvand, M., and Ilário, C., "Trailing Edge Bluntness Flow and Noise Control Using Porous Treatments," *22nd AIAA/CEAS Aeroacoustics Conference*, AIAA 2016-2832.

[15]Showkat Ali, S. A., Liu, X., and Azarpeyvand, M., "Bluff Body Flow and Noise Control Using Porous Media," *22nd AIAA/CEAS Aeroacoustics Conference*, AIAA 2016-2754.

[16]Showkat Ali, S. A., Azarpeyvand, M., da Silva, and Ilário, C., "Boundary Layer Interaction With Porous Surface and Implications For Aerodynamic Noise," *23rd International Congress on Sound & Vibration*, ICSV 2016.

[17]Liu, H., Azarpeyvand, M., Wei, J., and Qu, Z., "Tandem cylinder aerodynamic sound control using porous coating," *Journal of Sound and Vibration*, Vol. 334, 2015, pp. 190–201.

[18]Afshari, A., Azarpeyvand, M., Dehghan, A. A., and Szoke, M., "Trailing Edge Noise Reduction Using Novel Surface Treatments," *22nd AIAA/CEAS Aeroacoustics Conference*, AIAA 2016-2384.

[19]Afshari, A., Dehghan, A. A., Azarpeyvand, M., and Szőke, M., "Three-Dimentional Surface Treatments For Trailing Edge Noise Reduction," *22nd AIAA/CEAS Aeroacoustics Conference*, AIAA 2016-2384.

[20]Baker, J. P. and Van Dam, C., "Drag reduction of blunt trailing-edge airfoils," *BBAA VI International Colloquium on Bluff Bodies Aerodynamics & Applications*, 2008.

[21]Brooks, T. F. and Hodgson, T., "Trailing edge noise prediction from measured surface pressures," *Journal of sound and vibration*, Vol. 78, No. 1, 1981, pp. 69–117.

[22]Brooks, T. F., Pope, D. S., and Marcolini, M. A., *Airfoil self-noise and prediction*, Vol. 1218, National Aeronautics and Space Administration, Office of Management, Scientific and Technical Information Division, 1989.

[23]Roger, M. and Moreau, S., "Trailing edge noise measurements and prediction for subsonic loaded fan blades," *AIAA paper*, Vol. 2460, 2002.

[24]Hoerner, S. F. and Borst, H. V., "Fluid-dynamic lift: practical information on aerodynamic and hydrodynamic lift," 1985.

[25]Bearman, P. W. and Tombazis, N., "The effects of three-dimensional imposed disturbances on bluff body near wake flows," *Journal of Wind Engineering and Industrial Aerodynamics*, Vol. 49, No. 1, 1993, pp. 339–349.

[26]Tombazis, N. and Bearman, P., "A study of three-dimensional aspects of vortex shedding from a bluff body with a mild geometric disturbance," *Journal of Fluid Mechanics*, Vol. 330, 1997, pp. 85–112.

[27]Sato, J. and Sunada, Y., "Experimental research on blunt trailing-edge airfoil sections at low Reynolds numbers," *AIAA journal*, Vol. 33, No. 11, 1995, pp. 2001–2005.

[28]Thompson, B. and Lotz, R., "Flow around a blunt and divergent trailing edge," *Experiments in fluids*, Vol. 33, No. 3, 2002, pp. 374–383.

[29]Deshpande, P. and Sharma, S., "Spanwise vortex dislocation in the wake of segmented blunt trailing edge," *Journal of Fluids and Structures*, Vol. 34, 2012, pp. 202–217.

[30]Nati, G., Kotsonis, M., Ghaemi, S., and Scarano, F., "Control of vortex shedding from a blunt trailing edge using plasma actuators," *Experimental Thermal and Fluid Science*, Vol. 46, 2013, pp. 199–210.

[31]Standish, K. and Van Dam, C., "Aerodynamic analysis of blunt trailing edge airfoils," *Journal of Solar Energy Engineering*, Vol. 125, No. 4, 2003, pp. 479–487.

[32]Winnemöller, T. and Van Dam, C., "Design and numerical optimization of thick airfoils including blunt trailing edges," *Journal of Aircraft*, Vol. 44, No. 1, 2007, pp. 232–240.

[33]Bruneau, C.-H., Mortazavi, I., and Gilliéron, P., "Flow regularisation and drag reduction around blunt bodies using porous devices," *IUTAM Symposium on Flow Control and MEMS*, Springer, 2008, pp. 405–408.

[34]Bae, Y., Jeong, Y. E., and Moon, Y. J., "Effect of porous surface on the flat plate self-noise," *Proceedings of the 15th AIAA/CEAS Aeroacoustics Conference, AIAA-Paper*, No. 2009-3311, 2009.

[35]Bae, Y. and Moon, Y. J., "Effect of passive porous surface on the trailing-edge noise," *Physics of Fluids (1994-present)*, Vol. 23, No. 12, 2011, pp. 126101.

[36]Schulze, J. and Sesterhenn, J., "Optimal distribution of porous media to reduce trailing edge noise," *Computers & Fluids*, Vol. 78, 2013, pp. 41–53.

[37]Koh, S. R., Schröder, W., Meinke, M., Zhou, B. Y., and Gauger, N. R., "Noise sources of trailing-edge turbulence controlled by porous media," *20th AIAA/CEAS Aeroacoustics Conference. AIAA*, Vol. 3038, 2014, p. 2014.

[38]Zhou, B. Y., Gauger, N. R., Koh, S. R., Meinke, M., and Schröder, W., "On the Adjoint-based Control of Trailing-Edge Turbulence and Noise Minimization via Porous Material," *21st AIAA/CEAS Aeroacoustics Conference*, 2015, p. 2530.

[39]Rae, W. H. and Pope, A., *Low-speed wind tunnel testing*, John Wiley, 1984.

[40]Blake, W. K., *Mechanics of Flow-Induced Sound and Vibration V2: Complex Flow-Structure Interactions*, Vol. 2, Elsevier, 2012.

[41]Ozkan, G., Akilli, H., and Sahin, B., "Effect of High Porosity Screen on the Near Wake of a Circular Cylinder," *EPJ Web of Conferences*, Vol. 45, EDP Sciences, 2013, p. 01071.

[42]Ozkan, G. M. and Akilli, H., "Flow control around bluff bodies by attached permeable plates," *Int. J. Mech. Aerosp. Ind. Mechatron. Eng*, Vol. 8, No. 5, 2014, pp. 1035–1039.

[43]Bruneau, C.-H. and Mortazavi, I., "Numerical modelling and passive flow control using porous media," *Computers & Fluids*, Vol. 37, No. 5, 2008, pp. 488–498.

[44]Liu, H., Wei, J., and Qu, Z., "The Interaction of Porous Material Coating With the Near Wake of Bluff Body," *Journal of Fluids Engineering*, Vol. 136, No. 2, 2014, pp. 021302.

[45]Dupuit, J., *Etudes theoriques et pratiques sur le mouvement des eaux dans les canaux decouverts et a travers les terrains permeables avec des considerations relatives au regime des grandes eaux, au debouche a leur donner et a la marche des alluvions dans les rivieres a fond mobile*, Dunod, 1863.

[46]Theunissen, R., Di Sante, A., Riethmuller, M., and Van den Braembussche, R., "Confidence estimation using dependent circular block bootstrapping: application to the statistical analysis of PIV measurements," *Experiments in Fluids*, Vol. 44, No. 4, 2008, pp. 591–596.

[47]A/S, D. D., *Dantec Dynamics StreamWare Pro Installation and User Guide*, 5.11.00.14., 9040U4931, 2013.

[48]West, G. and Apelt, C., "The effects of tunnel blockage and aspect ratio on the mean flow past a circular cylinder with Reynolds numbers between 10 4 and 10 5," *Journal of Fluid Mechanics*, Vol. 114, 1982, pp. 361–377.

[49]Garcia-Sagrado, A. and Hynes, T., "Wall pressure sources near an airfoil trailing edge under turbulent boundary layers," *Journal of Fluids and Structures*, Vol. 30, 2012, pp. 3–34.

[50]Gruber, M., *Airfoil noise reduction by edge treatments*, Ph.D. thesis, University of Southampton, 2012.

[51]Corcos, G., "Resolution of pressure in turbulence," *The Journal of the Acoustical Society of America*, Vol. 35, No. 2, 1963, pp. 192–199.

[52]Gravante, S., Naguib, A., Wark, C., and Nagib, H., "Characterization of the pressure fluctuations under a fully developed turbulent boundary layer," *AIAA journal*, Vol. 36, No. 10, 1998, pp. 1808–1816.

[53]AKERNATHY, F. H., "Fundamentals of boundary layers," 1988.

[54]Lim, H.-C. and Lee, S.-J., "Flow control of a circular cylinder with O-rings," *Fluid Dynamics Research*, Vol. 35, No. 2, 2004, pp. 107–122.

[55]Bevilaqua, P. M., "Intermittency, the entrainment problem," 1973.

[56]Das, D., Nassehi, V., and Wakeman, R., "A finite volume model for the hydrodynamics of combined free and porous flow in sub-surface regions," *Advances in Environmental Research*, Vol. 7, No. 1, 2002, pp. 35–58.